7N -O2

194169

P-34

NASA

TECHNICAL NOTE

D-14

TRANSONIC AERODYNAMIC CHARACTERISTICS OF SEVERAL BODIES

HAVING ELLIPTICAL CROSS SECTIONS AND VARIOUS PLAN FORMS

By Robert A. Taylor

Ames Research Center
Moffett Field, Calif.

NATIONAL AERONAUTICS AND SPACE ADMINISTRATION

WASHINGTON   August 1959

U

NATIONAL AERONAUTICS AND SPACE ADMINISTRATION

TECHNICAL NOTE D-14

TRANSONIC AERODYNAMIC CHARACTERISTICS OF SEVERAL BODIES

HAVING ELLIPTICAL CROSS SECTIONS AND VARIOUS PLAN FORMS

By Robert A. Taylor

SUMMARY

The measured force characteristics are presented for a series of progressively shortened bodies having elliptical cross sections with major to minor axis ratios of 3 and 4. In addition, a body with a curved major axis, and a ratio of major to minor axes of 4 was tested. The bodies were tested through an angle-of-attack range from $-2°$ through $+12°$ and a Mach number range from 0.40 to 1.20. Reynolds number based on the length of the models varied from approximately 9×10^6 to 21×10^6.

INTRODUCTION

This investigation is part of a systematic program conducted in the Ames 14-foot transonic wind tunnel to determine the aerodynamic characteristics of bodies in the transonic speed range. In a previous report (ref. 1) the pressure and force measurements for a series of flattened bodies with elliptical cross sections with ratios of major to minor axes of 1.0, 1.5, 2.0, and 3.0 were presented.

The present report presents experimental force data for a series of progressively shortened bodies having elliptical cross sections with major to minor axis ratios of 3 and 4. In addition, a body with a curved major axis, and a ratio of major to minor axes of 4 was tested.

NOTATION

A   plan-form area

B   base area

C_D drag coefficient, $\dfrac{\text{drag}}{q_\infty A}$

C_L lift coefficient, $\dfrac{\text{lift}}{q_\infty A}$

C_m pitching-moment coefficient, $\dfrac{\text{moment about c.g.}}{q_\infty A}$

C_p pressure coefficient, $\dfrac{p - p_\infty}{q_\infty}$

c.g.   center of gravity

l body length from nose to point of closure

l_b truncated body length

M_∞ free-stream Mach number

p local static pressure

p_∞ free-stream static pressure

q_∞ free-stream dynamic pressure

r body radius

R Reynolds number based on l_b

α angle of attack, bodies pitched in plane of minor axis of elliptical cross section

ξ, η, θ cylindrical coordinate system (see sketch (a)) where ξ and η are normalized by dividing by l

H body radius normalized by dividing by l

λ ratio of major to minor axis of body cross section (see sketch (a))

Subscripts

1,2   major and minor axes of the elliptical cross section (see sketch (a))

av   average

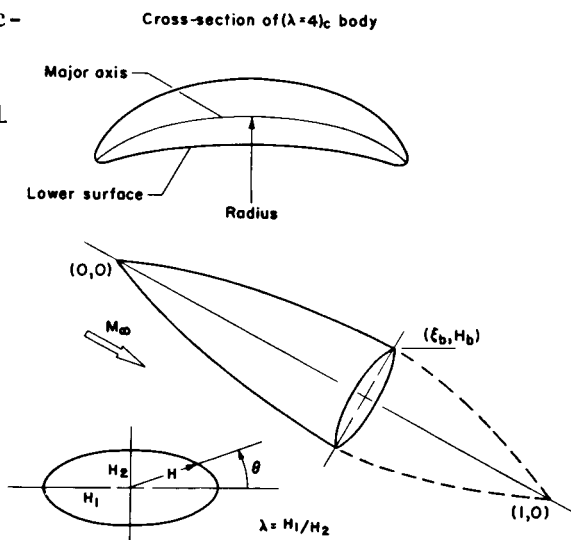b   body base

c   cambered

max   maximum

APPARATUS AND MODELS

Wind Tunnel

This investigation was conducted in the Ames 14-foot transonic wind tunnel, which is a closed-return tunnel equipped with a perforated test section permitting continuous operation from subsonic to low supersonic speeds. Each wall of the test section contains 16 longitudinal slots with each slot containing a corrugated strip as indicated in figure 1. The ratio of accumulated slot widths (minus the accumulated width of the corrugated inserts) to tunnel perimeter in the plane normal to the air stream is equal to 0.054 (usually referred to as the porosity factor).

MODELS

The eight models considered in this investigation constituted a series of flat bodies with elliptical cross sections. The ratios of major to minor axes of the bodies were $\lambda = 3$ and $\lambda = 4$. An additional set of models with $\lambda = 4$ were cambered by curving the major axis so that it was part of a circular arc whose radius was equal to 12.75 inches (see sketch (a)). The model series was developed from a parabolic-arc body of revolution with a fineness ratio of 12 (see ref. 1). The axial distribution of cross-sectional area was maintained as the bodies were distorted so as to have elliptical cross sections (except in the case of model $(\lambda=4)_c$). A further variation in plan form was attained by progressively truncating the bodies. Three plan forms were considered, the body base locations being $\xi = 0.58$, $\xi = 0.72$, and $\xi = 0.85$ (see figs. 2 and 3). Additional geometric characteristics are shown in the tabulation below. The centers of moments were located approximately at the centroid of the plan-form area.

Cross-section of $(\lambda=4)_c$ body

Major axis

Lower surface —

Radius

$(0,0)$

M_∞

(ξ_b, H_b)

H_2 H θ

H_1

$\lambda = H_1/H_2$

$(1,0)$

Sketch (a)

Configuration	$r_{1_{max}}$, in.	$r_{2_{max}}$, in.	l_b, in.	B, ft^2	A, ft^2	Centers of moments, $\% l_b$
$\lambda=3, \xi_b=0.85$	5.19	1.73	61.45	0.049	3.26	50
$\lambda=3, \xi_b=0.58$	5.19	1.73	41.60	.186	2.14	65
$\lambda=4, \xi_b=0.85$	6.00	1.50	61.45	.049	3.77	50
$\lambda=4, \xi_b=0.72$	6.00	1.50	51.60	.129	3.22	60
$\lambda=4, \xi_b=0.58$	6.00	1.50	41.60	.186	2.47	65
$(\lambda=4)_c, \xi_b=0.85$	6.00	1.50	61.45	.049	3.77	50
$(\lambda=4)_c, \xi_b=0.72$	6.00	1.50	51.60	.129	3.22	60
$(\lambda=4)_c, \xi_b=0.58$	6.00	1.50	41.60	.186	2.47	65

The normalized radii of the uncambered bodies are given by

$$H(\xi) = \frac{\sqrt{\lambda}\, \tilde{H}(\xi)}{\sqrt{\cos^2\theta + \lambda^2\sin^2\theta}} \tag{1}$$

where $\tilde{H}$ is the normalized radius of a body of revolution having identical cross-sectional area.

INSTRUMENTATION

The aerodynamic forces were measured by a strain-gage balance enclosed within the models. Multiple-tube manometers were photographed to record the pressure data. Orifices were located on the model base and in the cavity between the body and sting support in order to measure base pressures.

TESTS AND PROCEDURE

The uncambered models were tested at angles of attack varying from -2° to $+12^\circ$, the angle-of-attack range for the cambered body, $(\lambda=4)_c$, $\xi_b = 0.58$, varied from -10° to $+12^\circ$. Mach number was varied from 0.40 to 1.20 with a corresponding Reynolds number range of 9.0×10^6 to 21.0×10^6

(based on model length l_b), see figure 4. To fix transition, No. 28
Carborundum grits were cemented on the nose of each model.

The experimental data were not corrected for tunnel-wall inter-
ference effects. Considerations of the testing procedure and the data-
reduction process indicate that the free-stream Mach numbers are repeat-
able within ±0.002, the angle of attack is accurate within ±0.1°, and
the pressure coefficient data are repeatable within ±0.005.

The experimental data are believed to be affected by sting-support
interference, the magnitudes of which are not fully known. From the
existing data at zero angle of attack for bodies of revolution (refs.
2 and 3), an estimate of sting-support effects was made. The study as
applied to lift-drag ratios at $\alpha = 6^\circ$ (near $(L/D)_{max}$) for the bodies
with $\xi = 0.85$, indicated the L/D values were 7 percent too high.

The force and pressure data were obtained simultaneously and
reduced to standard coefficient form.

DATA PRESENTATION

The data presented in this report consist of longitudinal force
and moment characteristics at various Mach numbers and angles of attack.

Force Data

The basic lift, drag, and pitching-moment data for the models are
presented in figures 5 through 11. The drag coefficients have not been
adjusted to represent free-stream static pressure at the base of each
model. The average base-drag coefficients are tabulated and presented
in table I. Cross plots of longitudinal characteristics as a function
of Mach number and angle of attack are presented in figures 12 through
20.

Figure 12 shows the variation of lift coefficient with Mach number.
Figure 13 indicates the variation of pitching moment with Mach number.
The variations of drag coefficient with Mach number are shown in figure
14. The variations in lift, drag, and pitching moment with Mach number
at the negative angles of attack for the $(\lambda=4)_c$, $\xi_b = 0.58$ model are
presented in figure 15. Figure 16 indicates the variation of base-drag
coefficient with Mach number at constant angles of attack for the differ-
ent configurations. The variations of lift-drag ratio with Mach number
at several angles of attack are presented in figures 17 through 19.
Figure 20 indicates the variations in lift-drag ratio with angle of

attack at Mach numbers of 0.90 and 1.20. Locations of the center of pressure (with respect to the model nose) are presented in figure 21 for angles of attack from 2° to 8°.

Ames Research Center
National Aeronautics and Space Administration
Moffett Field, Calif., Mar. 20, 1959

REFERENCES

1. McDevitt, John B., and Taylor, Robert A.: Force and Pressure Measurements at Transonic Speeds for Several Bodies Having Elliptical Cross Sections. NACA TN 4362, 1958.

2. Taylor, Robert A., and McDevitt, John B.: Pressure Distributions at Transonic Speeds for Parabolic-Arc Bodies of Revolution Having Fineness Ratios of 10, 12, and 14. NACA TN 4234, 1958.

3. Cahn, Maurice S.: An Experimental Investigation of Sting Support Effects on Drag and a Comparison with Jet Effects at Transonic Speeds. NACA RM L56F18a, 1956.

TABLE I.- TABULATION OF BASE DRAG COEFFICIENT

M_∞	α, deg	$\lambda = 3$ $\xi_b = 0.85$	$\lambda = 3$ $\xi_b = 0.58$	$\lambda = 4$ $\xi_b = 0.85$	$\lambda = 4$ $\xi_b = 0.72$	$\lambda = 4$ $\xi_b = 0.58$	$(\lambda=4)_c$ $\xi_b = 0.85$	$(\lambda=4)_c$ $\xi_b = 0.72$	$(\lambda=4)_c$ $\xi_b = 0.58$
0.40	-10								0.0174
	-8								.0166
	-4								.0140
	-2		0.0141	0.0001	0.0043	0.0112	-0.0003	0.0040	.0129
	0		.0135	0	.0041	.0110	-.0002	.0040	.0123
	2		.0140	0	.0042	.0112	-.0002	.0040	.0129
	4		.0152	.0001	.0045	.0120	-.0002	.0044	.0135
	6		.0171	.0002	.0051	.0138	0	.0048	.0144
	8		.0195	.0004	.0059	.0151	.0002	.0057	.0161
	10		.0208	.0005	.0067	.0160	.0004	.0066	.0183
	12		.0217	.0005	.0070	.0167	.0004	.0075	
.60	-10								.0174
	-8								.0166
	-4								.0145
	-2		.0144	.0002	.0046	.0115	-.0002	.0046	.0134
	0		.0140	.0001	.0043	.0112	-.0003	.0041	.0129
	2		.0142	.0002	.0045	.0116	-.0003	.0041	.0132
	4		.0154	.0003	.0051	.0126	-.0003	.0045	.0140
	6		.0174	.0002	.0057	.0145	-.0001	.0050	.0182
	8		.0199	.0005	.0064	.0157	.0002	.0058	.0169
	10		.0212	.0006	.0072	.0165	.0003	.0068	.0189
	12		.0221	.0007	.0074	.0170	.0005	.0116	.0205
.90	-10								.0207
	-8								.0202
	-4								.0177
	-2		.0168	0		.0052	.0139	-.0004	.0049
	0	-0.0001	.0163	0		.0049	.0135	-.0008	.0046
	2	-.0001	.0167	0		.0050	.0142	-.0007	.0047
	4	0	.0175	.0001		.0056	.0154	-.0005	.0052
	6	-.0001	.0203	.0003		.0063	.0169	-.0002	.0057
	7				.0069				
	8		.0229	.0005		.0184	-.0001	.0070	.0195
	9			.0005					
	10		.0243			.0197	0	.0079	.0219
	11								.0232
	12		.0254				.0001	.0086	
.95	-10								.0226
	-8								.0221
	-4								.0198
	-2		.0184	-.0001	.0053	.0158	-.0006	.0052	.0179
	0		.0176	-.0001	.0050	.0153	-.0003	.0047	.0171
	2		.0182	-.0001	.0052	.0160	-.0006	.0048	.0175
	4		.0199	0	.0058	.0174	-.0005	.0052	.0184
	6		.0224	.0002	.0064	.0190	-.0004	.0058	.0192
	7				.0071				
	8		.0251	.0004		.0204	-.0002	.0068	.0217
	10		.0268			.0221	0	.0082	.0244
	12		.0283				0	.0088	.0255
.975	0	-.0006							
	2	-.0003							
	4	-.0003							
	6	-.0001							

TABLE I.- TABULATION OF BASE DRAG COEFFICIENT - Concluded

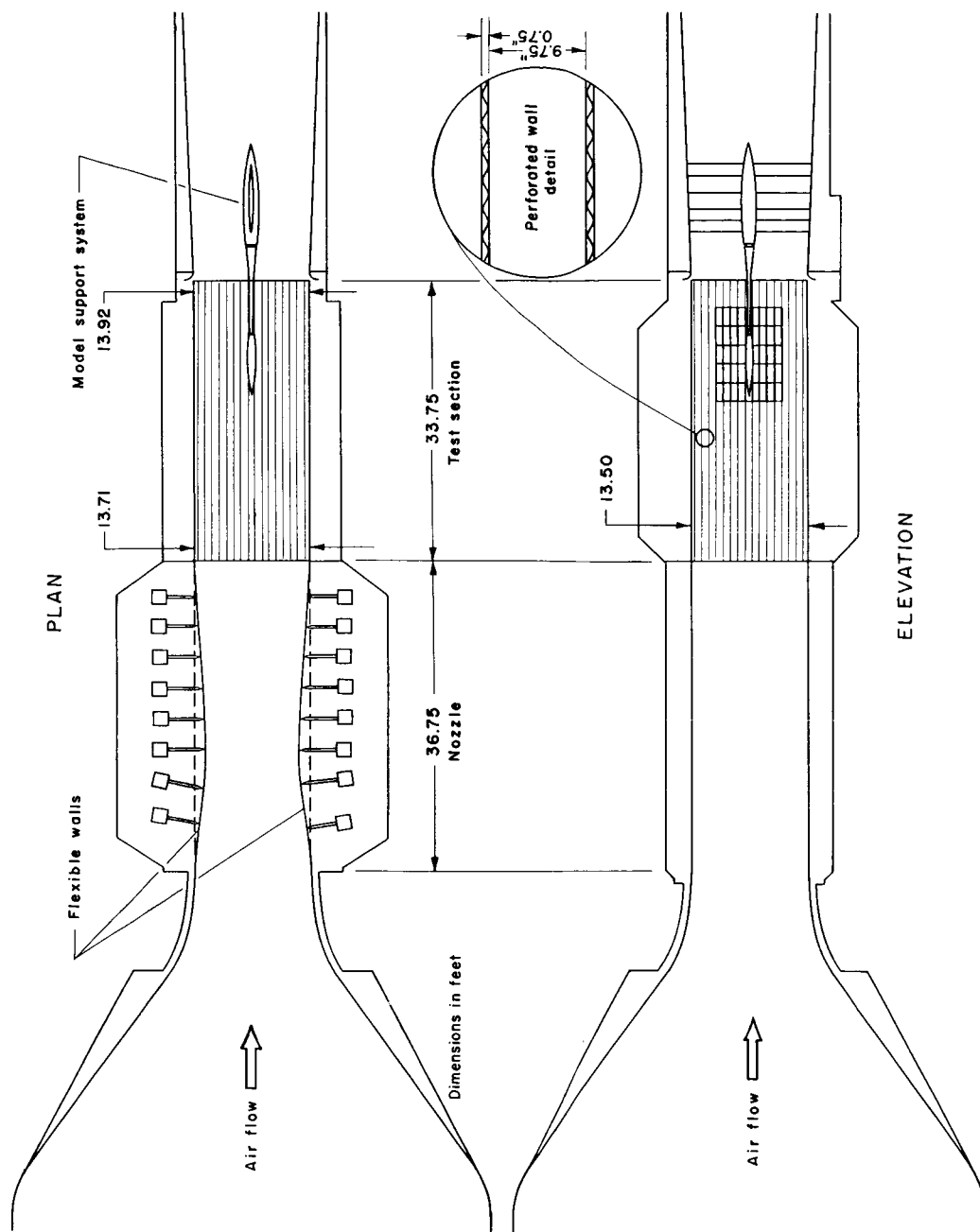| M_∞	α, deg	$\lambda = 3$ $\xi_b = 0.85$	$\lambda = 3$ $\xi_b = 0.58$	$\lambda = 4$ $\xi_b = 0.85$	$\lambda = 4$ $\xi_b = 0.72$	$\lambda = 4$ $\xi_b = 0.58$	$(\lambda=4)_c$ $\xi_b = 0.85$	$(\lambda=4)_c$ $\xi_b = 0.72$	$(\lambda=4)_c$ $\xi_b = 0.58$
1.00	-9								0.0303
	-8								.0295
	-4								.0264
	-2		0.0262	-0.0005	0.0059	0.0230	-0.0010	0.0047	.0249
	0	-0.0001	.0251	-.0005	.0053	.0222	-.0010	.0044	.0239
	2	0	.0255	-.0004	.0055	.0230	-.0010	.0045	.0234
	4	-.0001	.0272	-.0005	.0061	.0258	-.0009	.0049	.0255
	6	-.0002	.0307	-.0002	.0070	.0273	-.0008	.0056	.0264
	8		.0335	0		.0294	-.0006	.0068	.0287
	10		.0351			.0311	-.0005	.0080	.0324
	12		.0366				-.0005	.0091	
1.025	0	-.0001							
	2	0							
	4	-.0001							
	6	-.0002							
1.05	-9								.0326
	-8								.0319
	-4								.0287
	-2		.0262	-.0005	.0110	.0243	.0005	.0107	.0283
	0		.0251	-.0005	.0108	.0235	.0003	.0104	.0270
	2		.0255	-.0004	.0110	.0241	.0003	.0107	.0270
	4		.0272	-.0005	.0118	.0256	.0005	.0115	.0278
	6		.0307	-.0002	.0129	.0278	.0006	.0122	.0296
	8		.0335	0		.0297	.0010	.0133	.0326
	9					.0308			
	10		.0351				.0012	.0149	.0357
	12		.0366				.0013	.0160	
1.10	-9								.0310
	-8								.0310
	-4								.0287
	-2		.0274	.0006	.0104	.0241	.0002	.0097	.0271
	0	.0005	.0261	.0006	.0101	.0236	.0002	.0097	.0260
	2	.0005	.0274	.0008	.0104	.0243	.0002	.0098	.0258
	4	.0008	.0295	.0009	.0112	.0258	.0003	.0103	.0272
	6	.0009	.0323	.0012	.0121	.0279	.0006	.0120	.0290
	7				.0014				
	8		.0340			.0293	.0009	.0121	.0314
	9					.0303			
	10		.0357				.0011	.0136	.0341
	11							.0143	
	12		.0369				.0012		
1.20	-9								.0291
	-8								.0297
	-4								.0281
	-2		.0266	.0010	.0106	.0230	.0005	.0097	.0265
	0	.0010	.0255	.0010	.0104	.0224	.0005	.0099	.0255
	2	.0010	.0266	.0011	.0107	.0231	.0005	.0100	.0256
	4	.0012	.0289	.0013	.0112	.0244	.0006	.0104	.0268
	5								
	6	.0014	.0313	.0016	.0119	.0260	.0009	.0112	.0286
	7				.0017				
	8		.0328			.0273	.0012	.0124	.0302
	9					.0278			
	10		.0340				.0015	.0136	.0322
	11							.0142	
	12		.0349				.0016		

Figure 1.- General arrangement of the test section of the Ames 14-foot transonic wind tunnel.

A-24043

Figure 2.- Photograph of the $\lambda = 4$, $\xi_b = 0.85$ body mounted in the test section of the Ames 14-foot transonic wind tunnel.
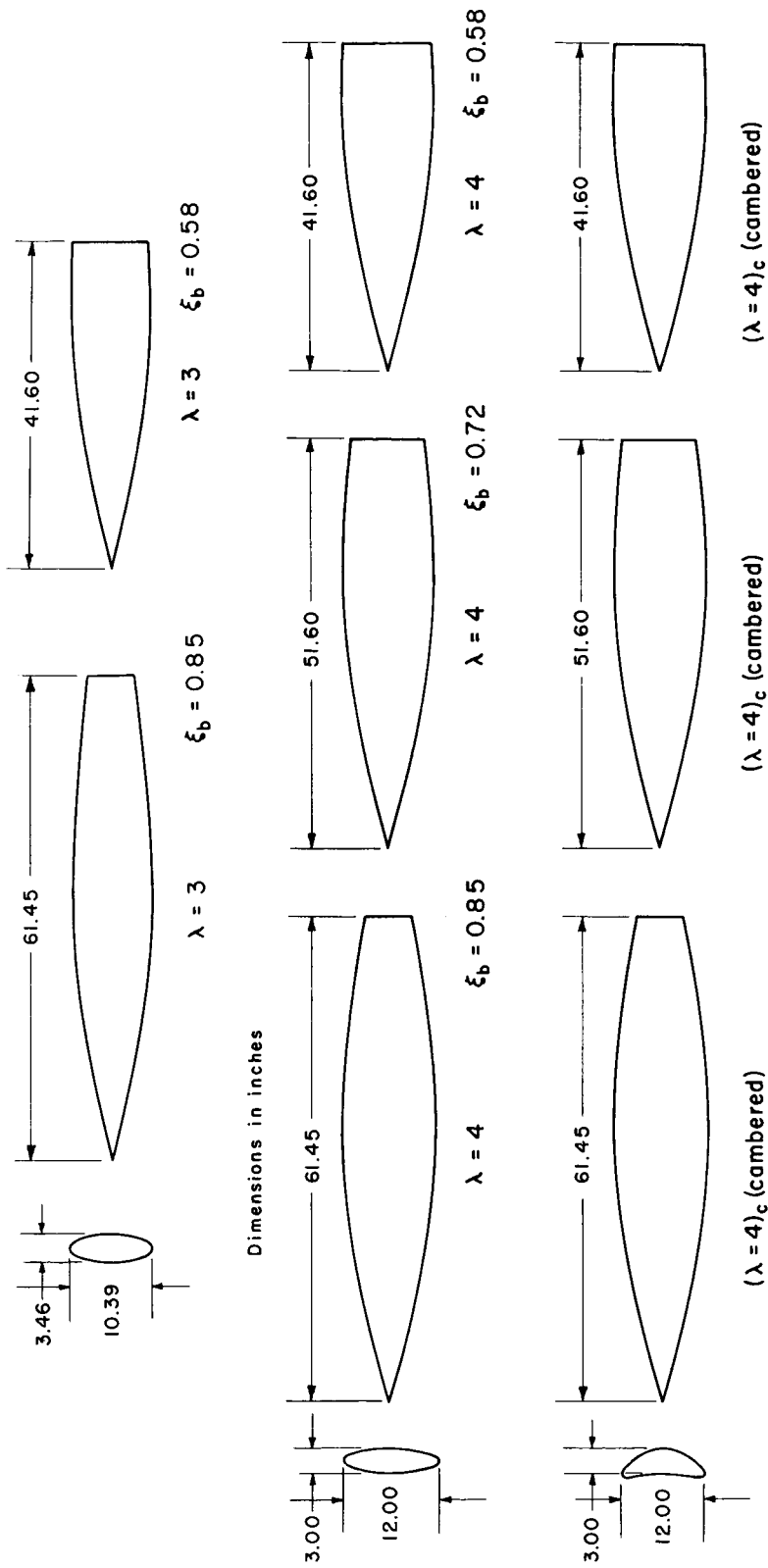
$\lambda = 3$ $\xi_b = 0.58$

$\lambda = 3$ $\xi_b = 0.85$

Dimensions in inches

$\lambda = 4$ $\xi_b = 0.58$

$\lambda = 4$ $\xi_b = 0.72$

$\lambda = 4$ $\xi_b = 0.85$

$(\lambda = 4)_c$ (cambered)

$(\lambda = 4)_c$ (cambered)

$(\lambda = 4)_c$ (cambered)

41.60

61.45

3.46

10.39

41.60

51.60

61.45

3.00

12.00

41.60

51.60

61.45

3.00

12.00

Figure 3.- Geometric details of the models.
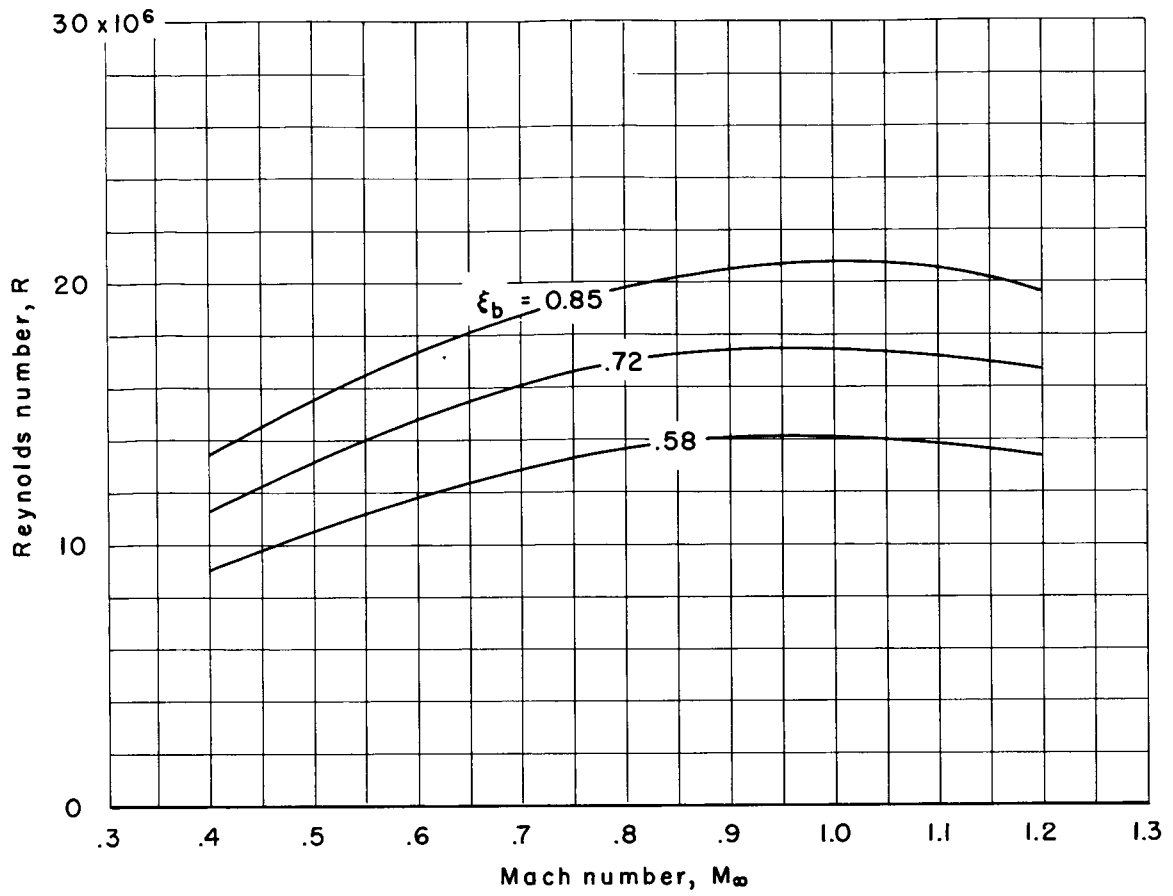
Figure 4.- Variation of Mach number with Reynolds number based on truncated body length.
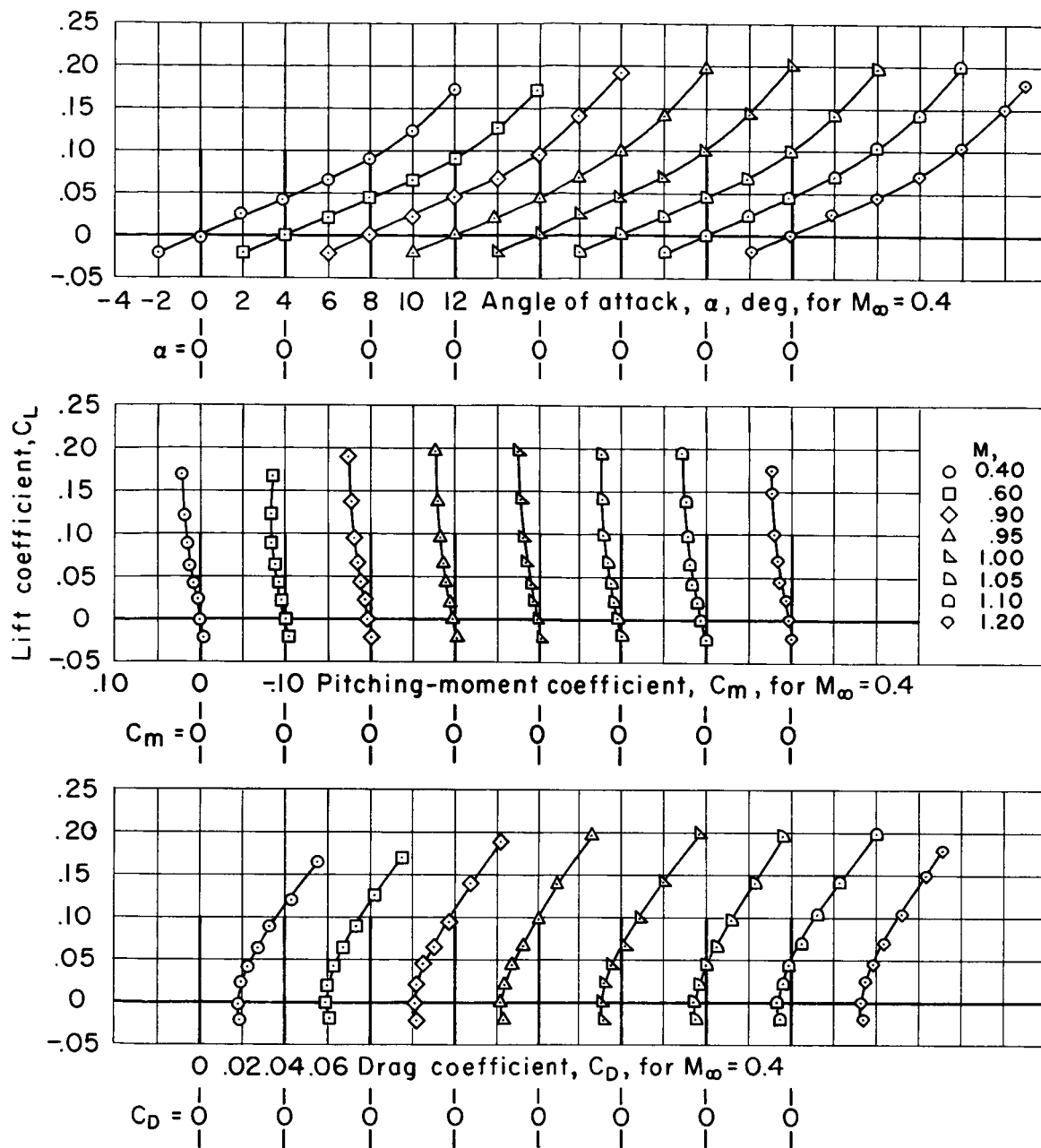
Figure 5.- Lift, drag, and pitching-moment characteristics of the $\lambda = 3$, $\xi_b = 0.58$ body.
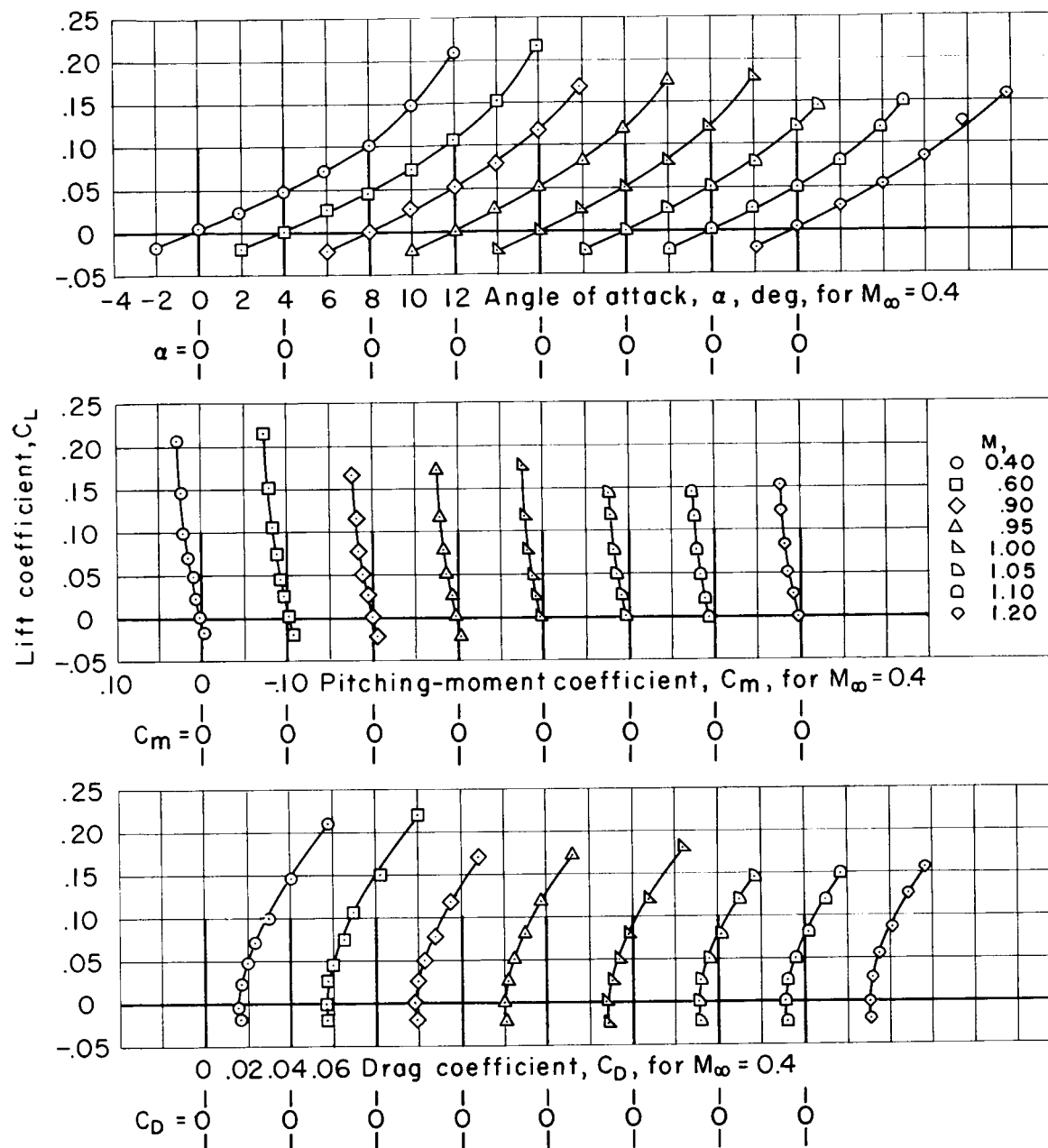
Figure 6.- Lift, drag, and pitching-moment characteristics of the $\lambda = 4$, $\xi_b = 0.58$ body.
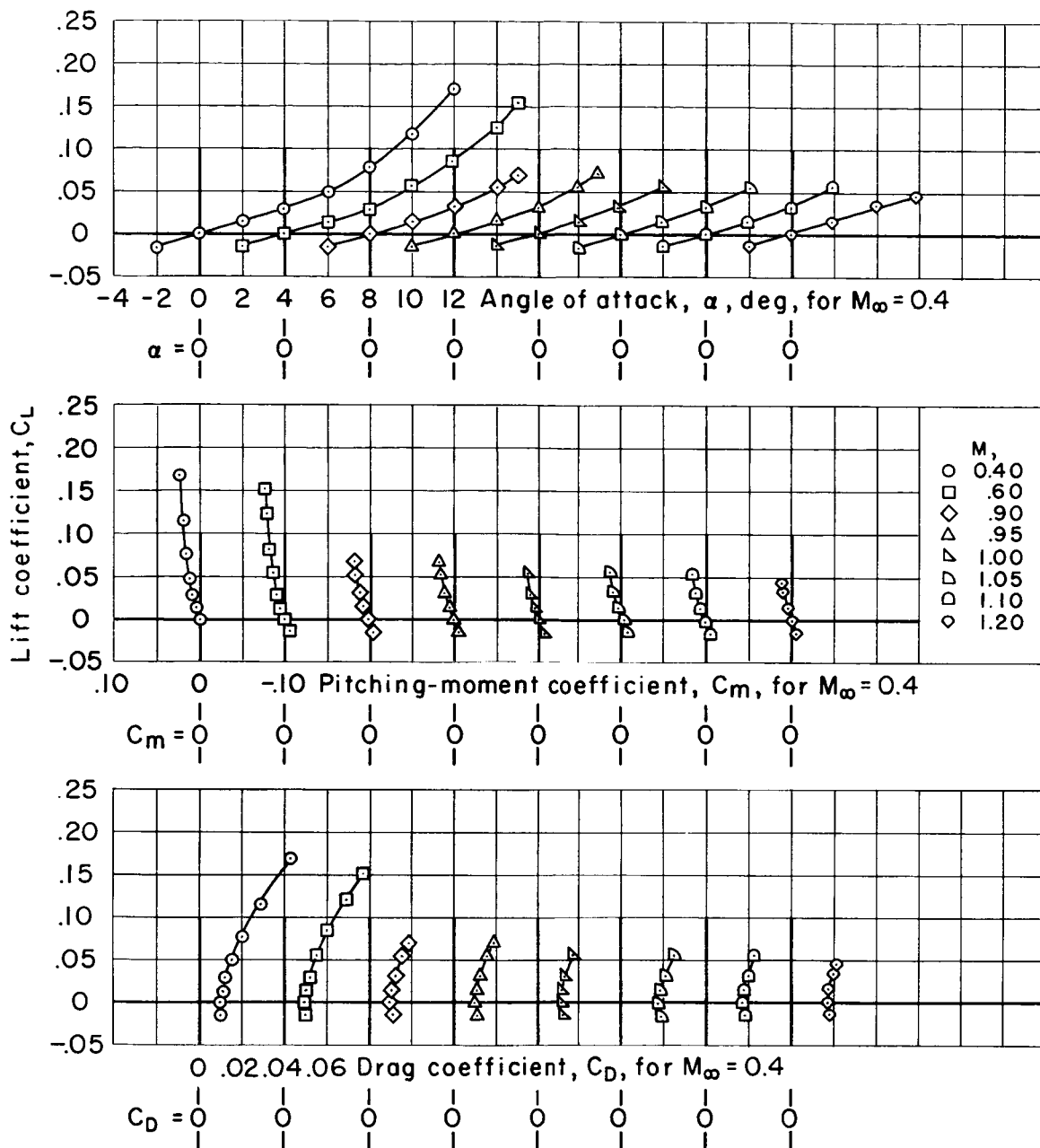
Figure 7.- Lift, drag, and pitching-moment characteristics of the $\lambda = 4$, $\xi_b = 0.72$ body.

16
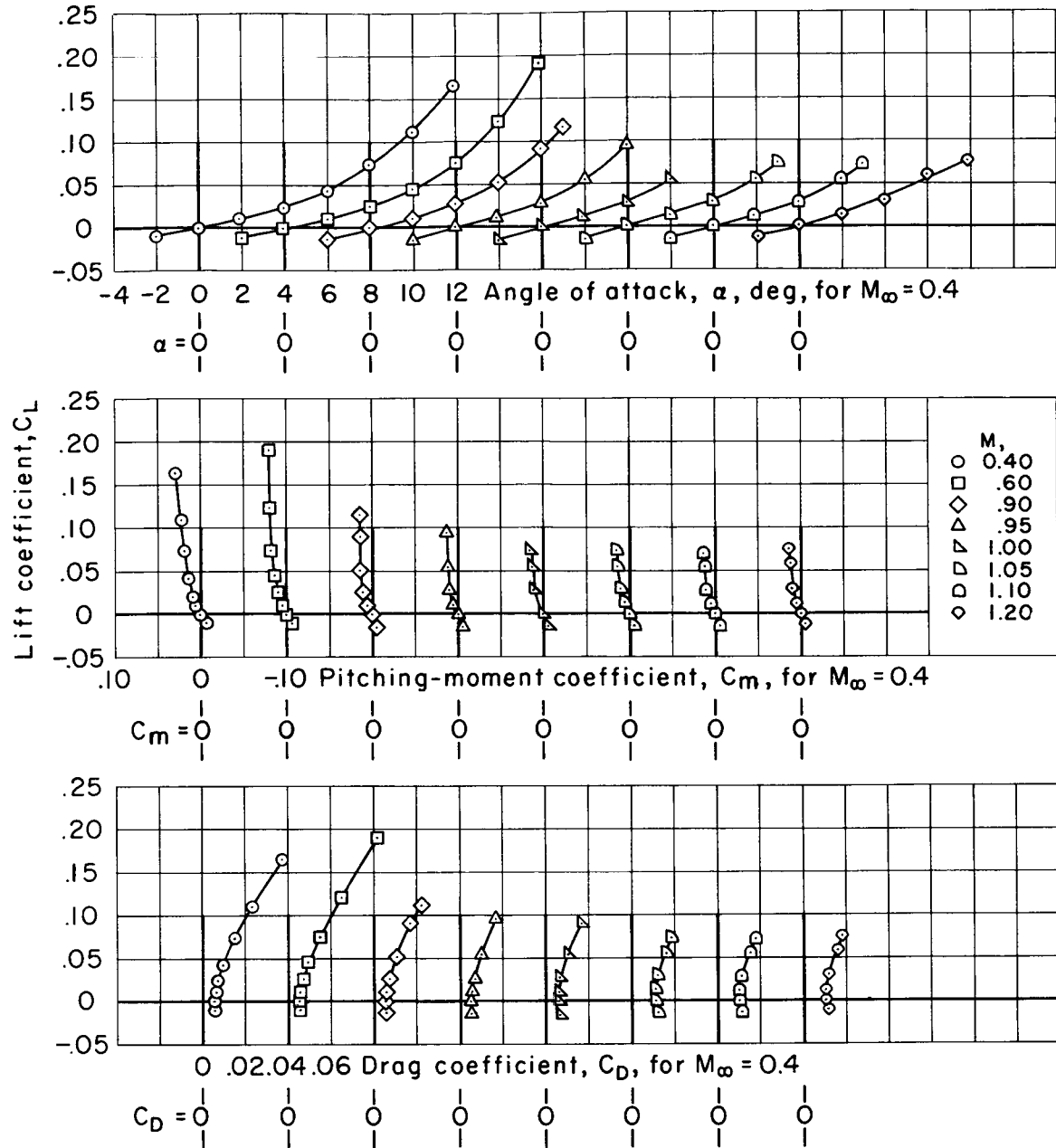
Figure 8.- Lift, drag, and pitching-moment characteristics of the $\lambda = 4$, $\xi_b = 0.85$ body.
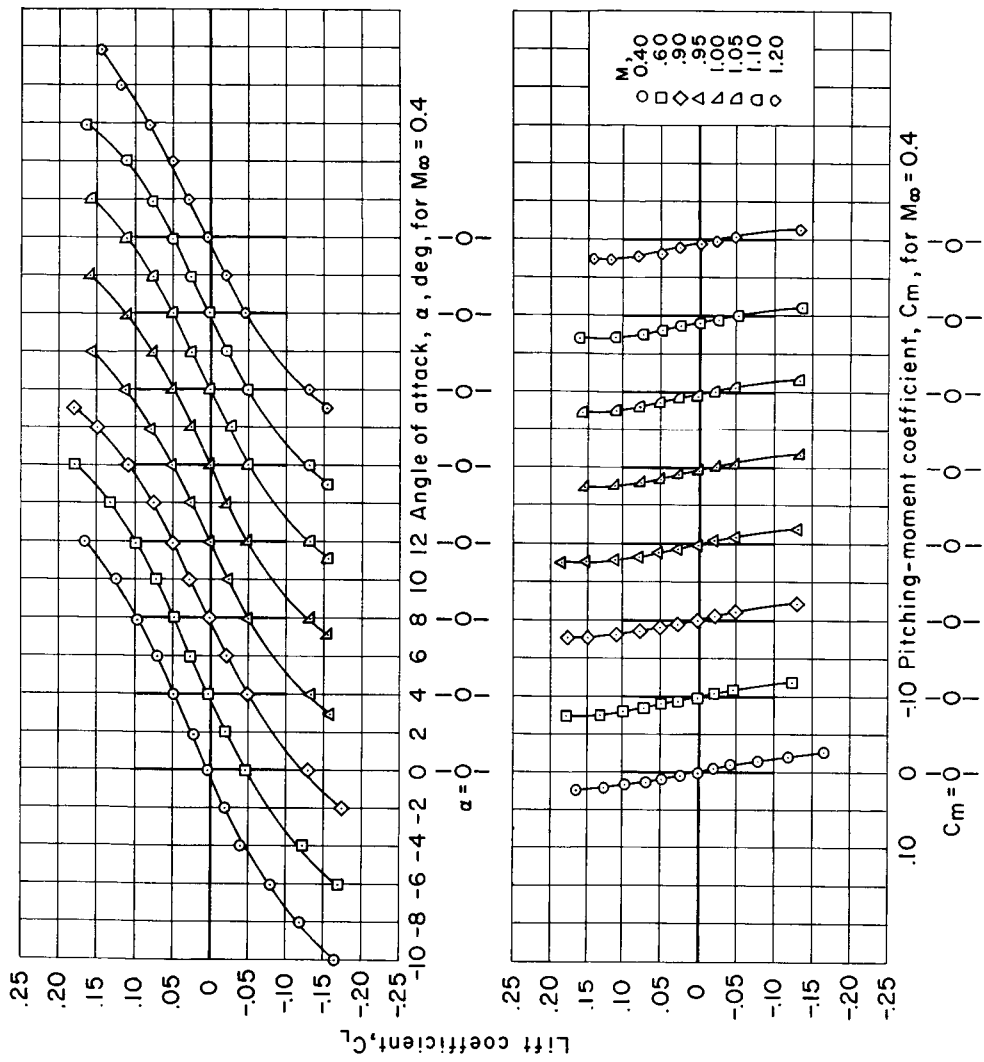
Figure 9.- Lift, drag, and pitching-moment characteristics of the $(\lambda=4)_c$, $\xi_b = 0.58$ body.
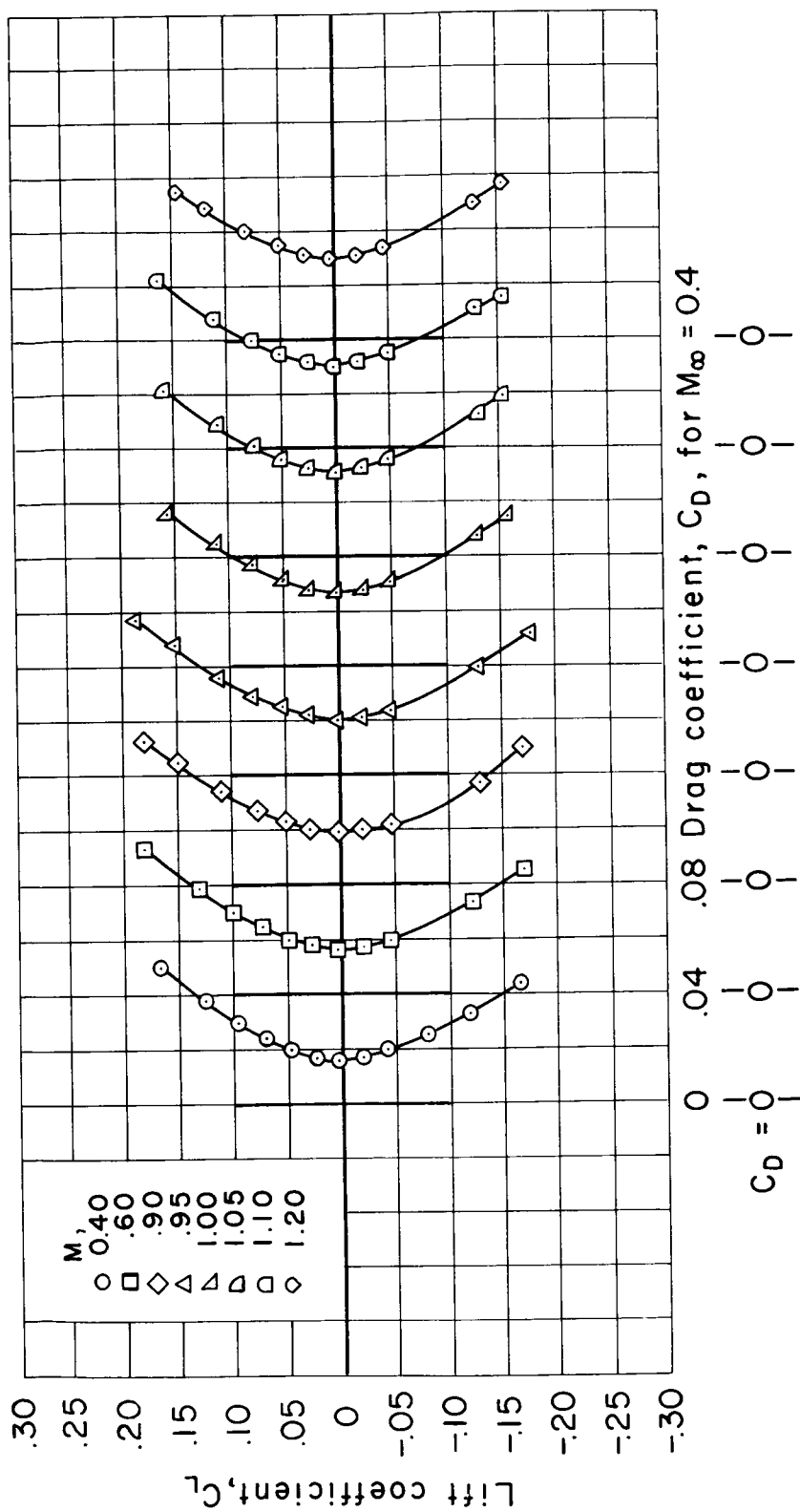
Figure 9.- Concluded.
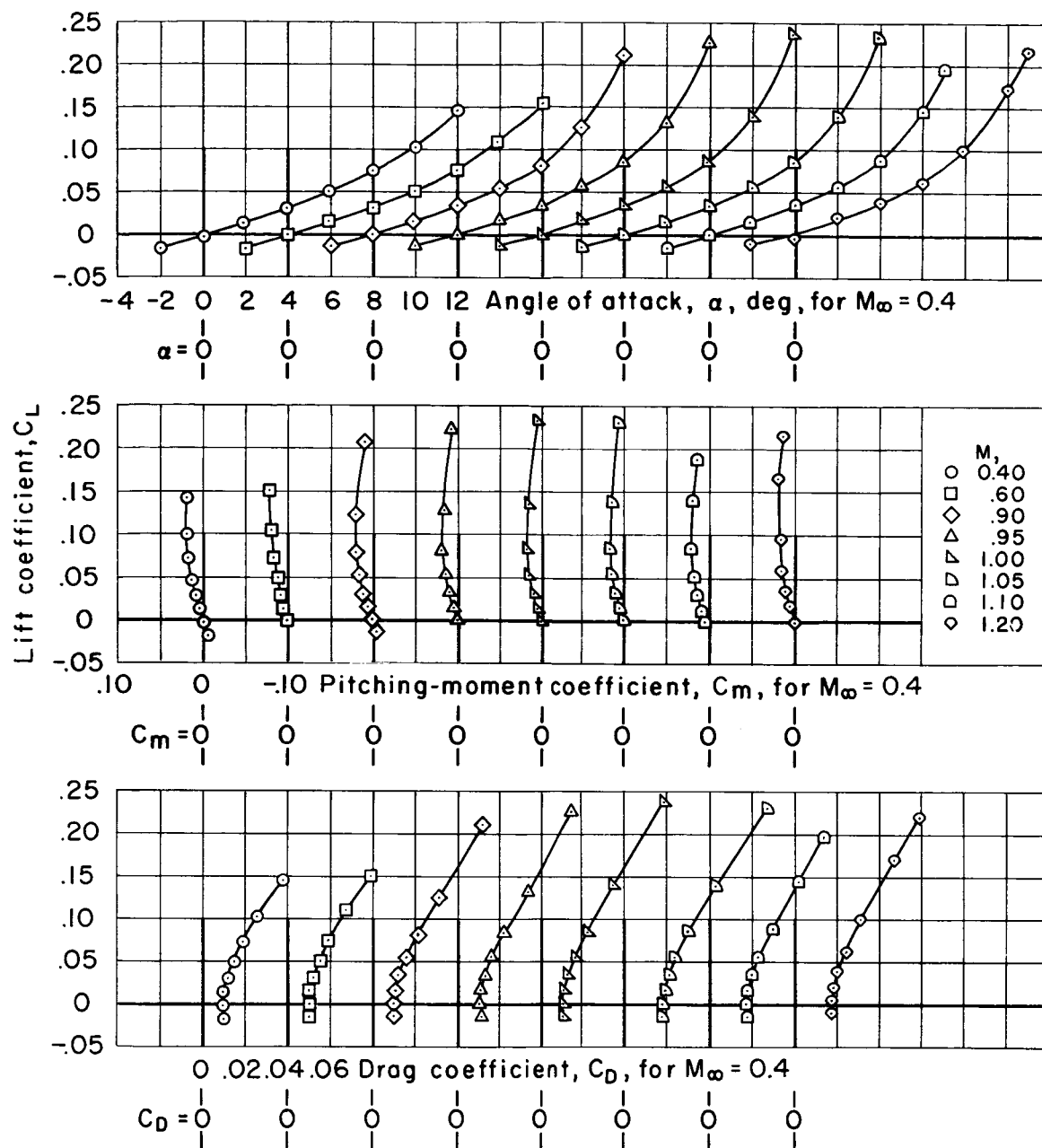
Figure 10.- Lift, drag, and pitching-moment characteristics of the $(\lambda=4)_c$, $\xi_b = 0.72$ body.
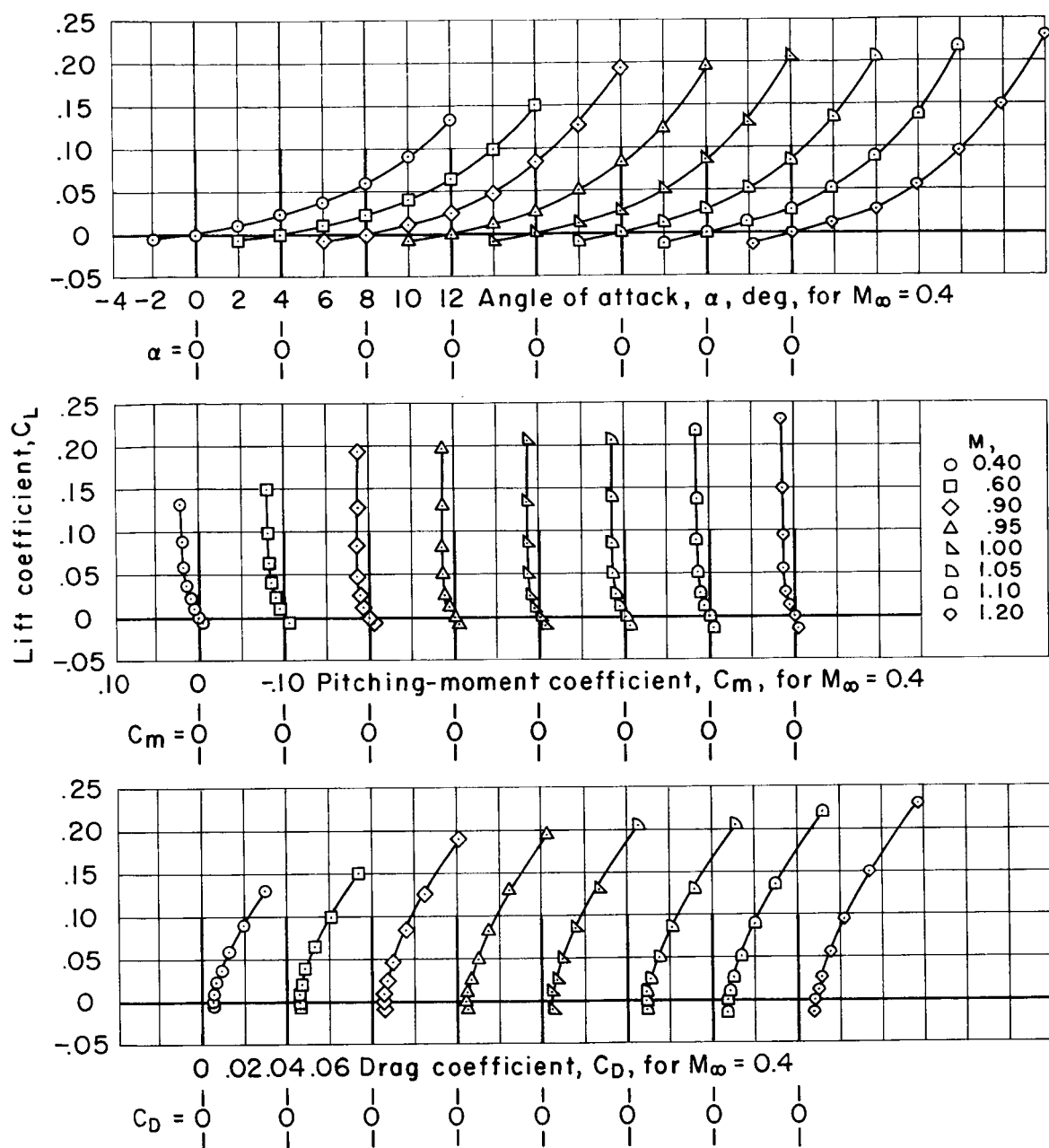
Figure 11.- Lift, drag, and pitching-moment characteristics of the $(\lambda=4)_c$, $\xi_b = 0.85$ body.
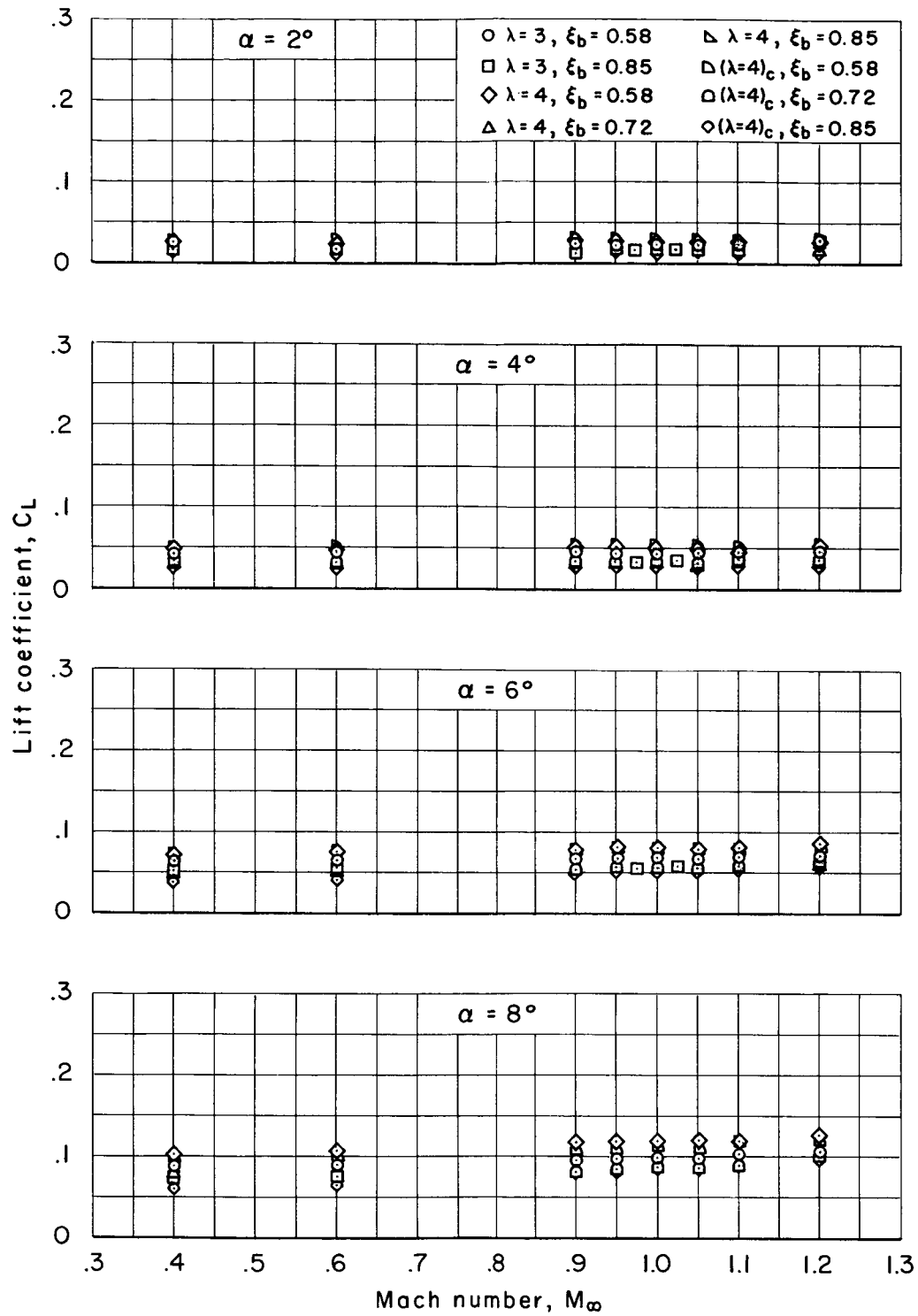
Figure 12.- Variation of lift coefficient with Mach number at various angles of attack.

22
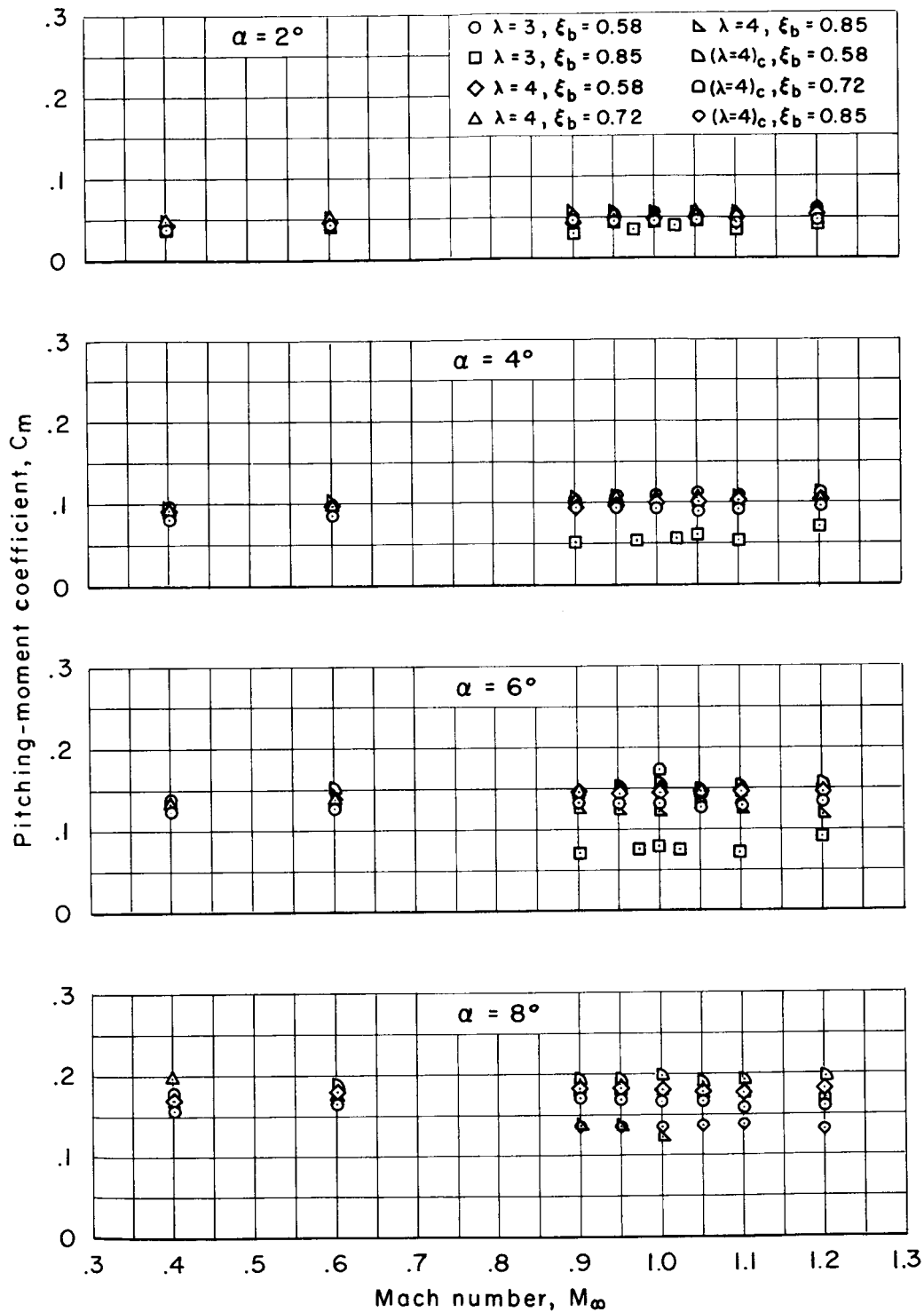
Figure 13.- Variation of pitching-moment coefficient with Mach number at various angles of attack.
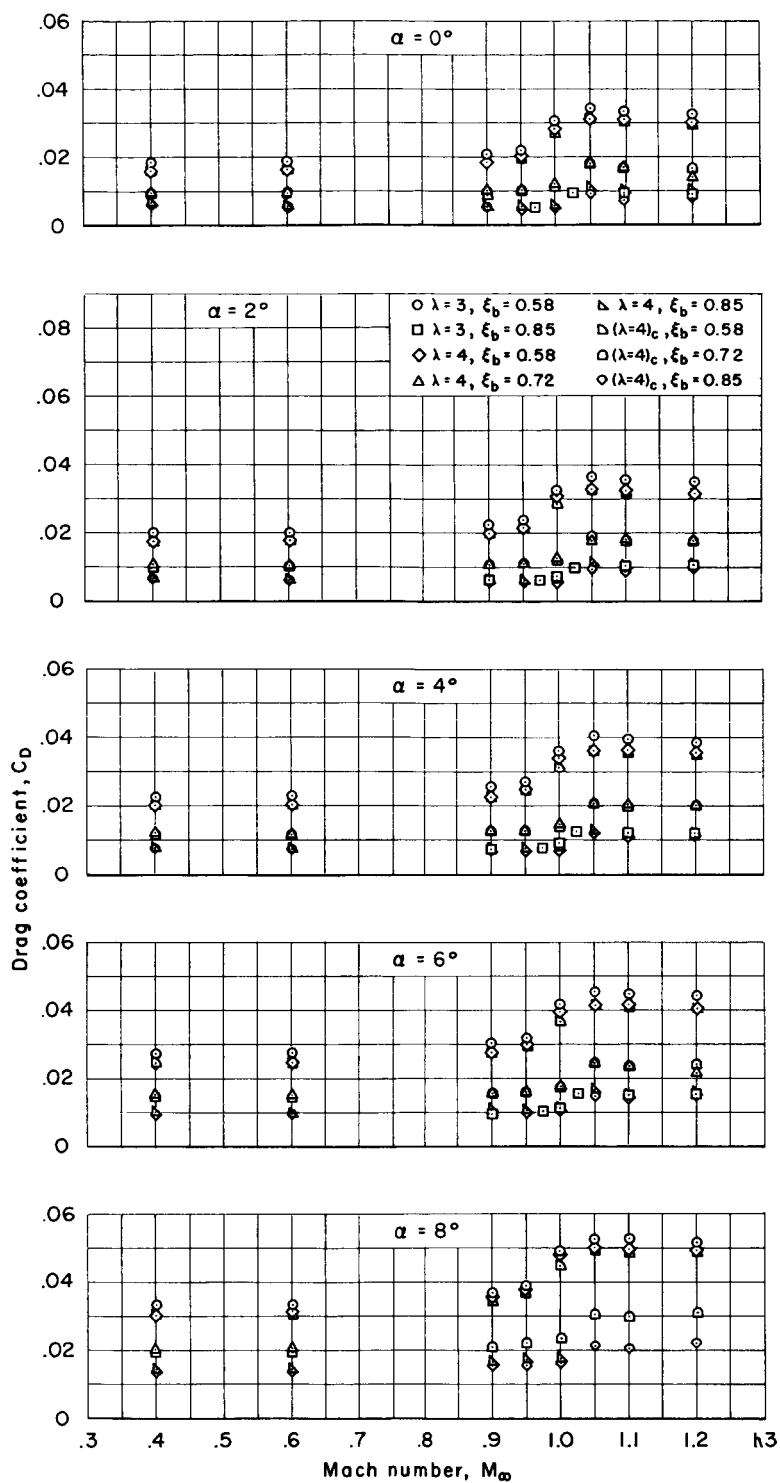
Figure 14.- Variation of drag coefficient with Mach number at various angles of attack.
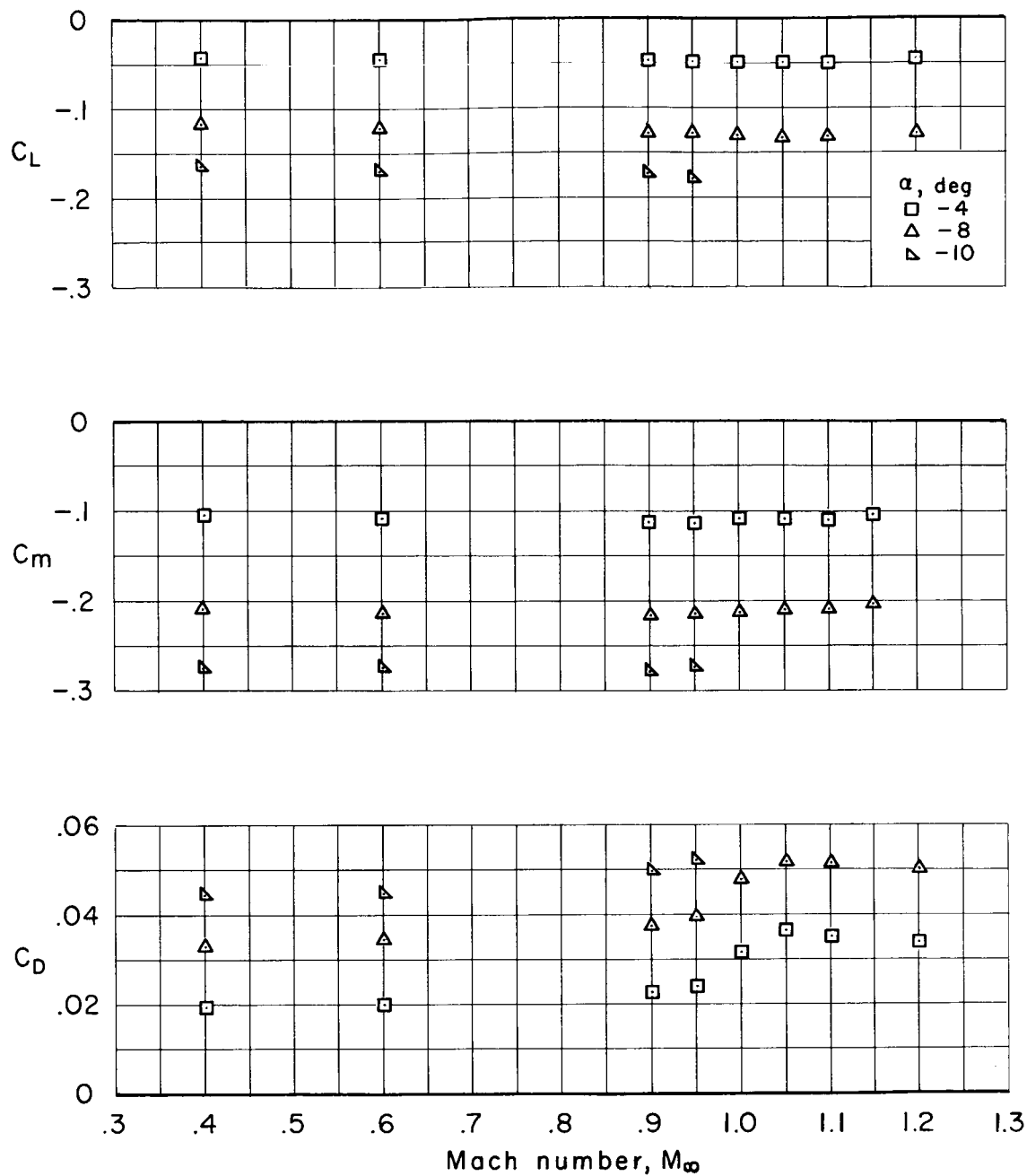
Figure 15.- Variation of lift, drag, and pitching-moment coefficient with Mach number at negative angles of attack for the $(\lambda=4)_c$, $\xi_b = 0.58$ body.
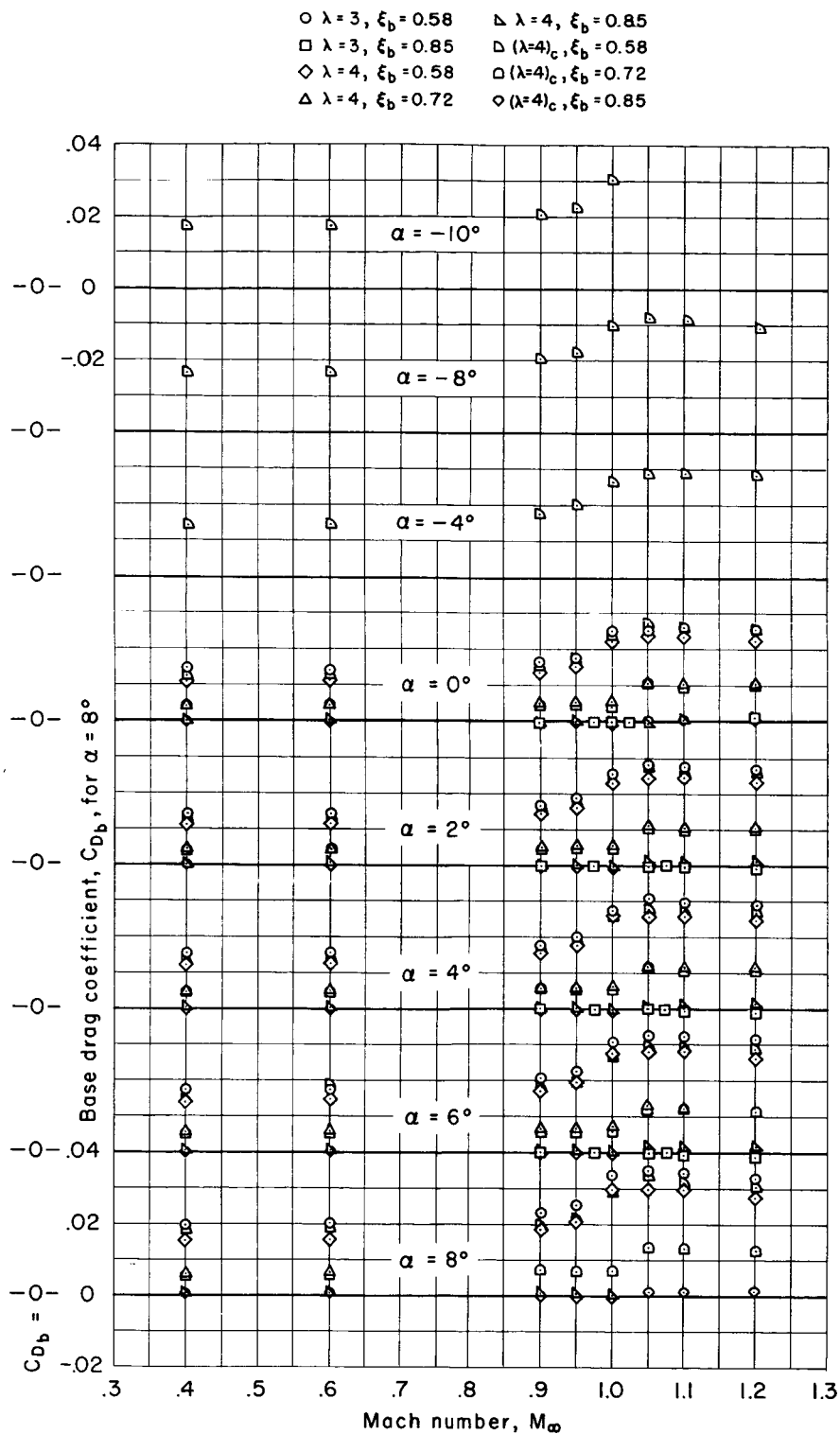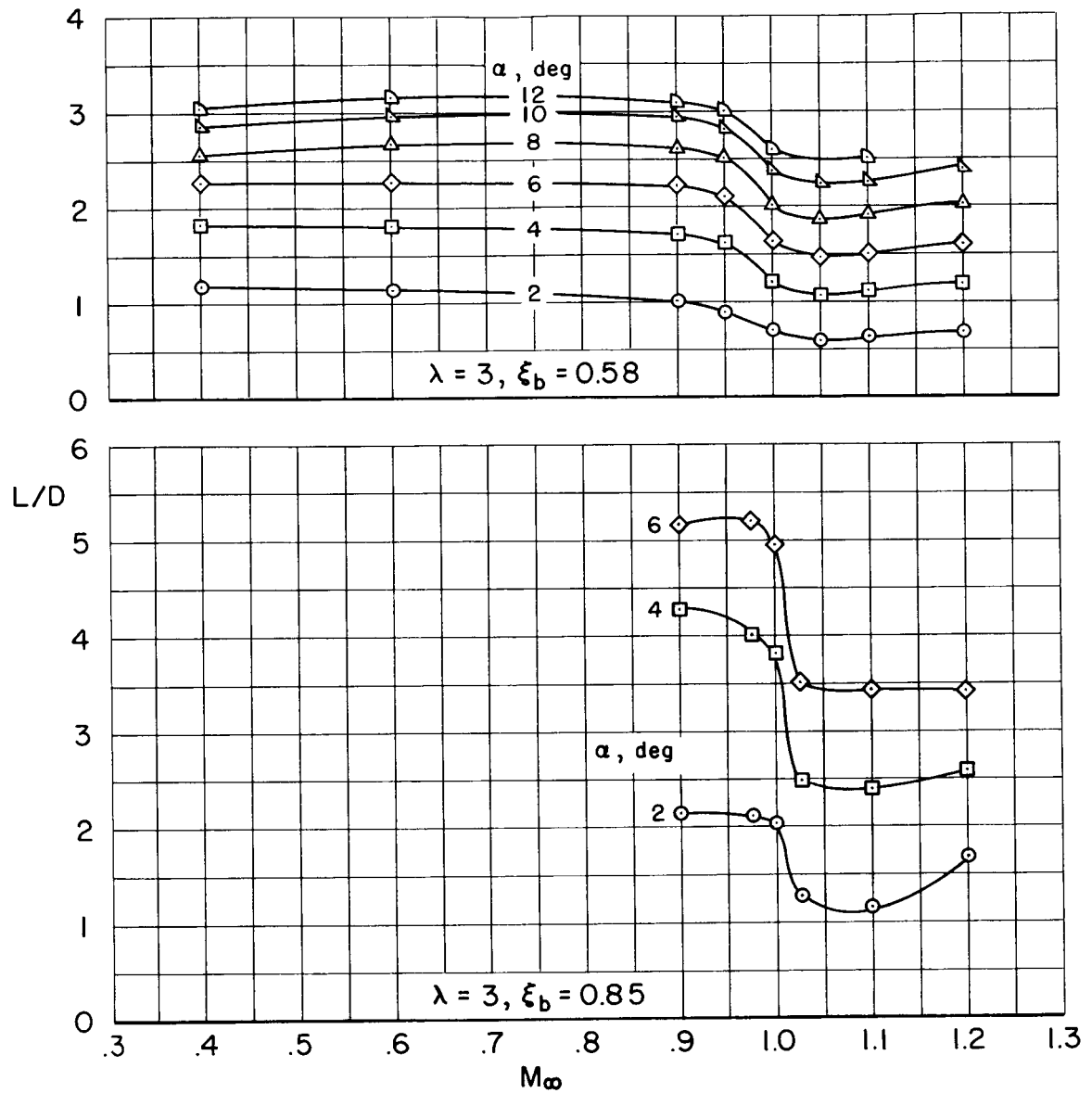
○ $\lambda = 3$, $\xi_b = 0.58$ ◺ $\lambda = 4$, $\xi_b = 0.85$
□ $\lambda = 3$, $\xi_b = 0.85$ ◿ $(\lambda = 4)_c$, $\xi_b = 0.58$
◇ $\lambda = 4$, $\xi_b = 0.58$ ◹ $(\lambda = 4)_c$, $\xi_b = 0.72$
△ $\lambda = 4$, $\xi_b = 0.72$ � $(\lambda = 4)_c$, $\xi_b = 0.85$

.04

.02

$\alpha = -10°$

−0− 0

−.02

$\alpha = -8°$

−0−

$\alpha = -4°$

−0−

$\alpha = 0°$

−0−

$\alpha = 2°$

−0−

$\alpha = 4°$

−0−

$\alpha = 6°$

−0− .04

.02

$\alpha = 8°$

−0− 0

$C_{D_b} =$ −.02

Base drag coefficient, C_{D_b}, for $\alpha = 8°$

.3   .4   .5   .6   .7   .8   .9   1.0   1.1   1.2   1.3

Mach number, M_∞

Figure 16.- Variation of base-drag coefficient with Mach number at
various angles of attack.

Figure 17.- Variation of lift-drag ratio with Mach number at various angles of attack for the $\lambda = 3$ body.
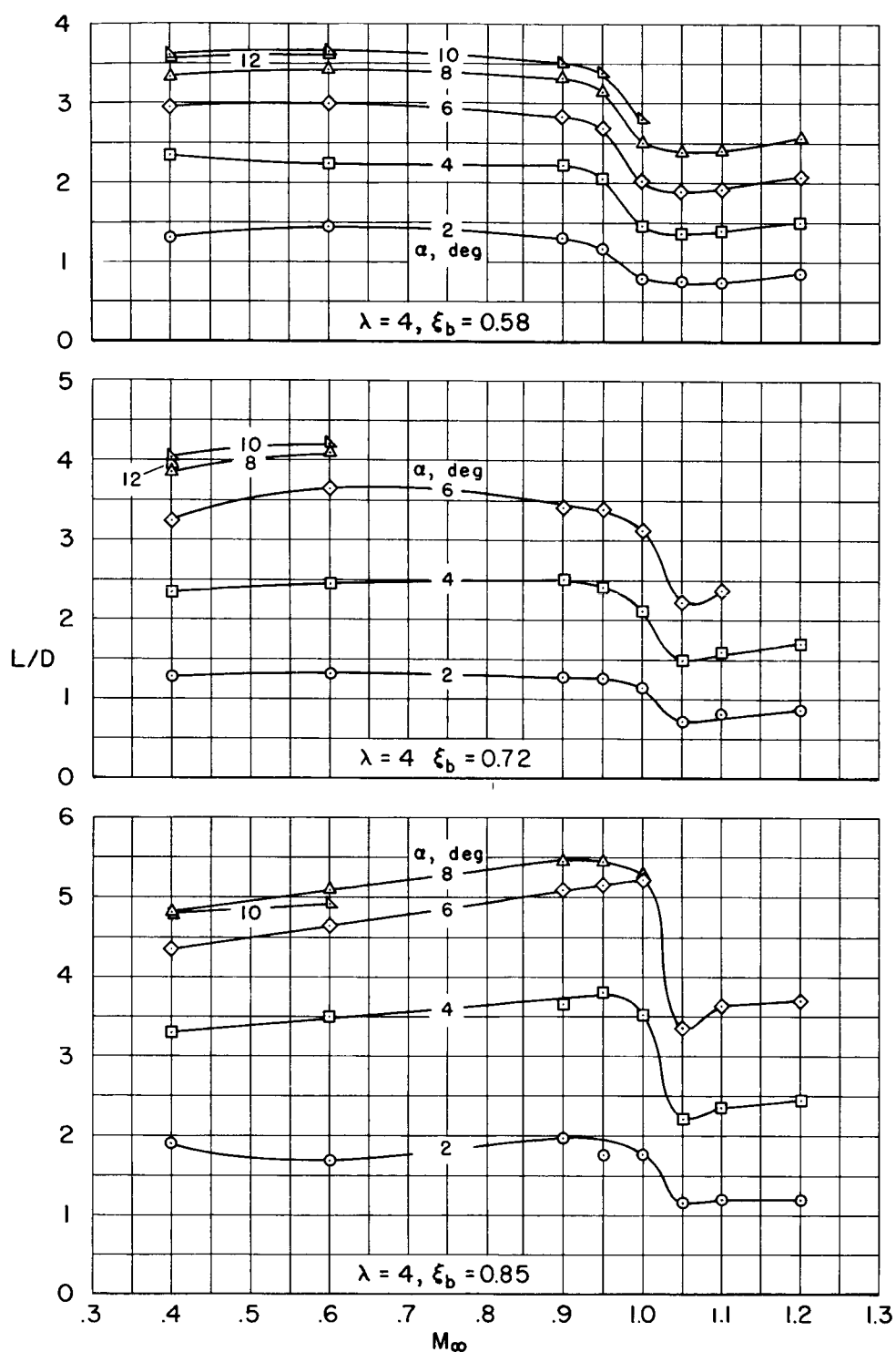
Figure 18.- Variation of lift-drag ratio with Mach number at various angles of attack for the $\lambda = 4$ body.
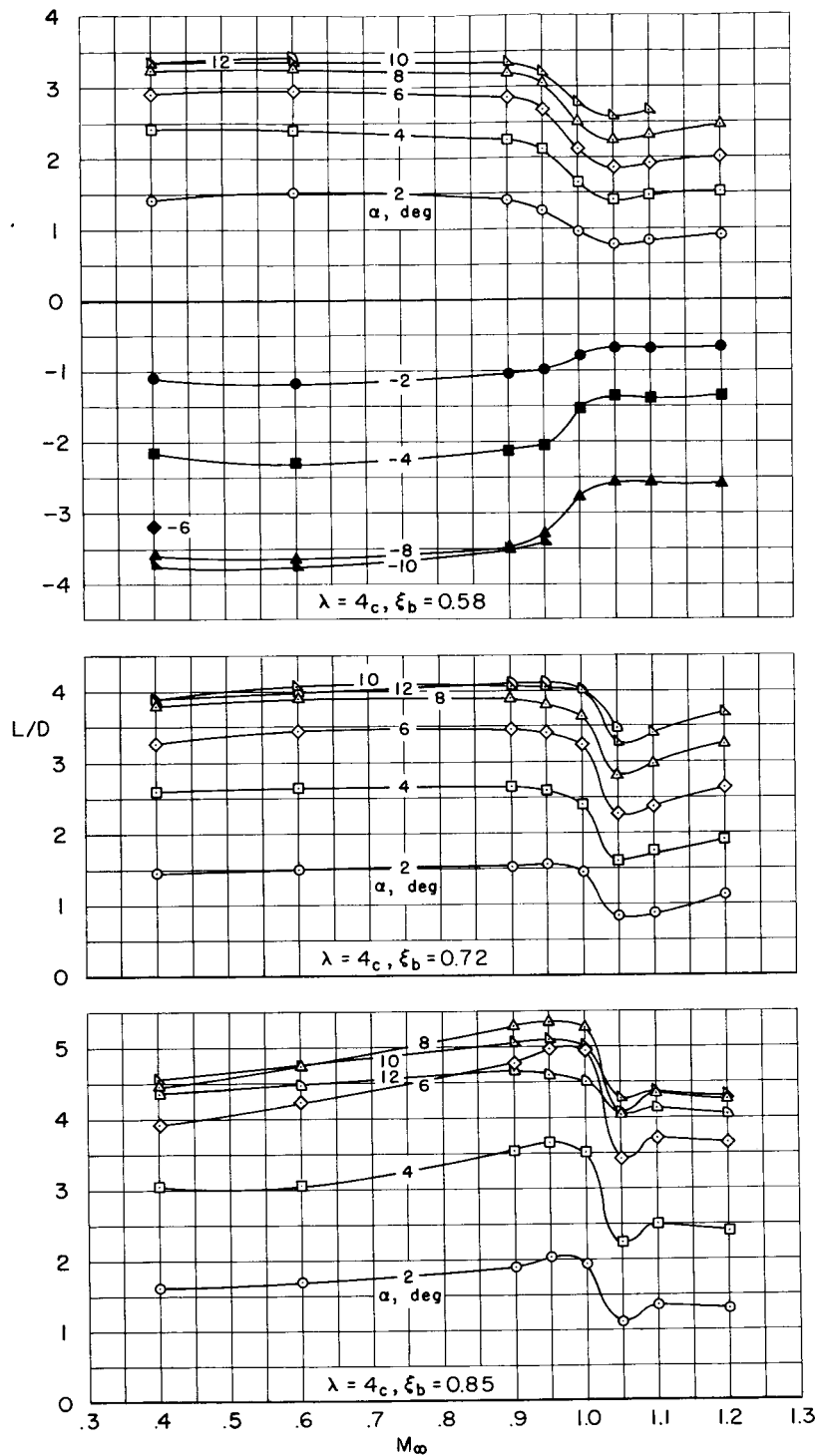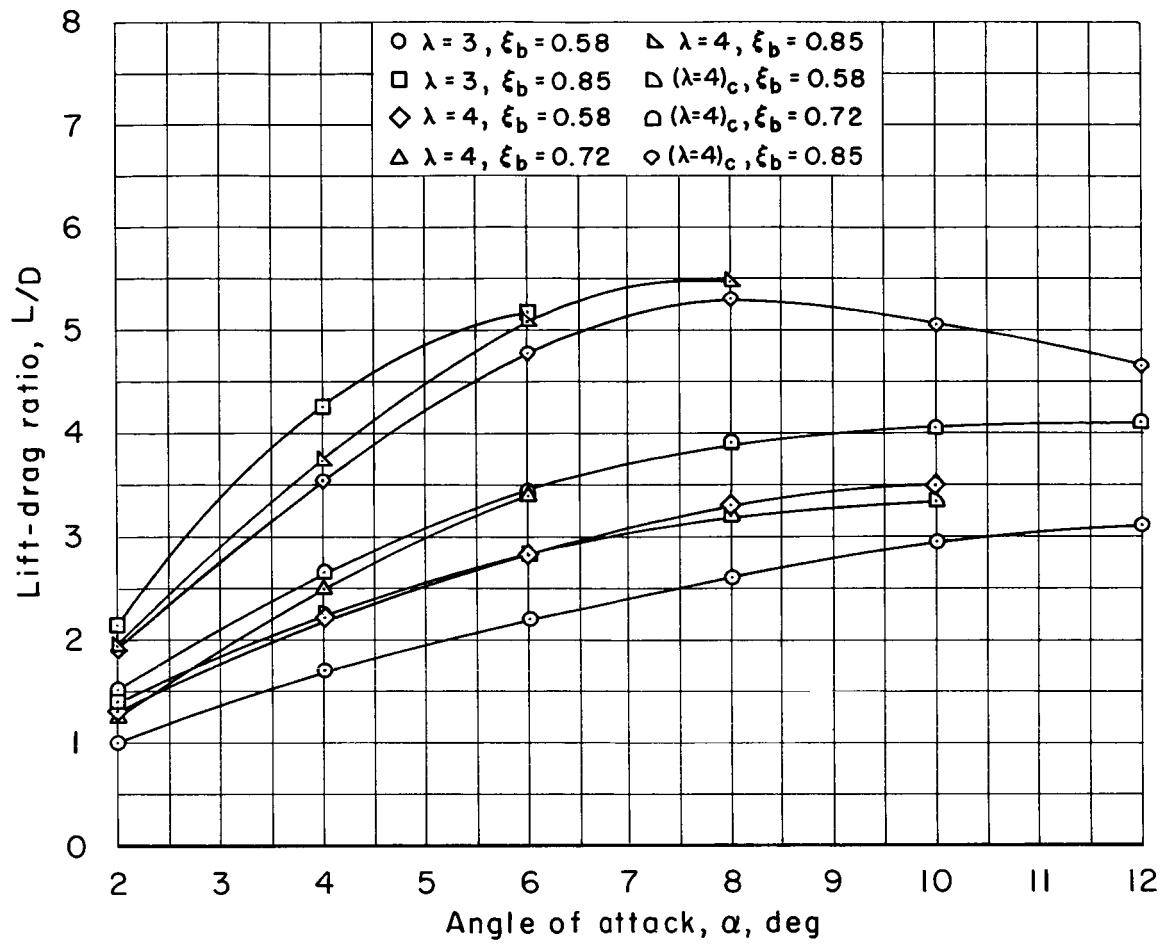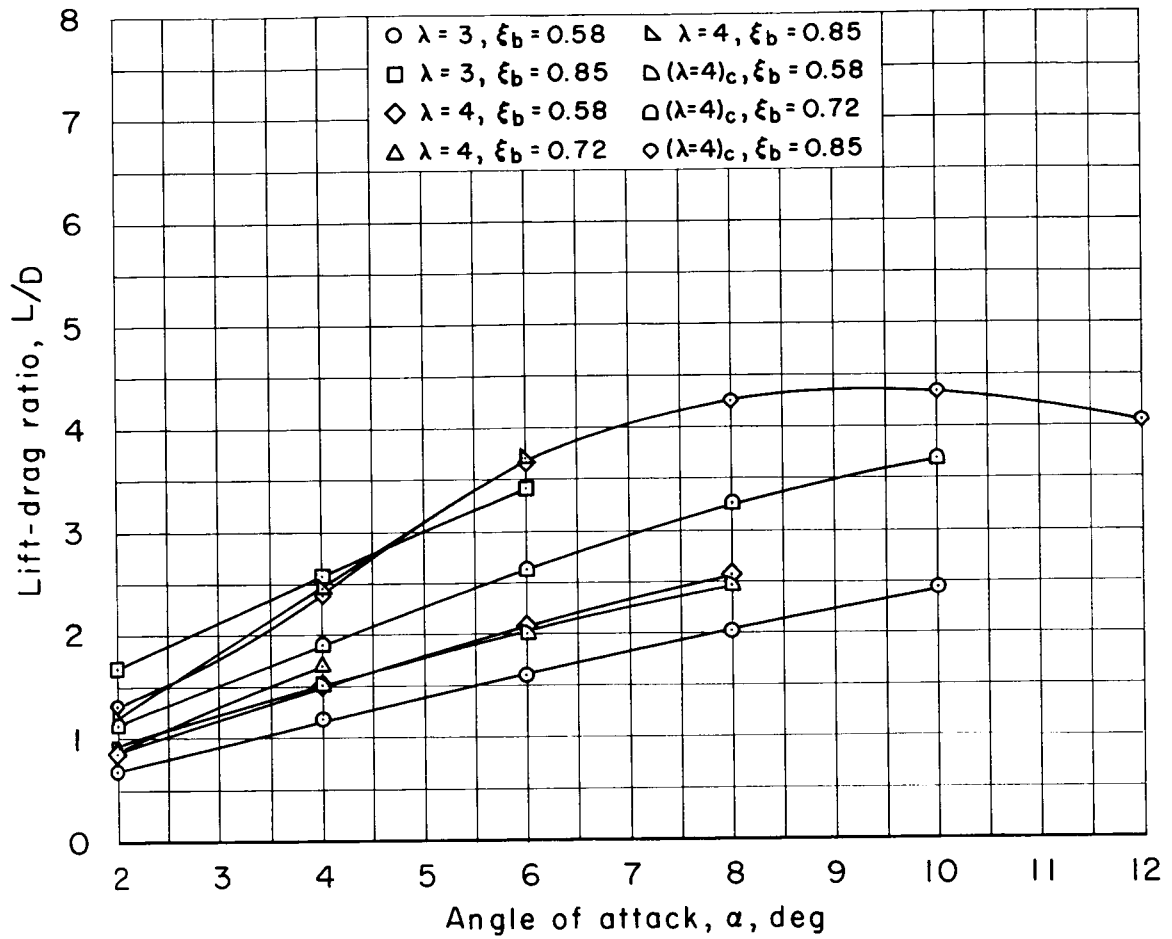
Figure 19.- Variation of lift-drag ratio with Mach number at various angles of attack for the $(\lambda=4)_c$ body.

(a) $M_\infty = 0.90$

Figure 20.- Variation of lift-drag ratio with angle of attack.
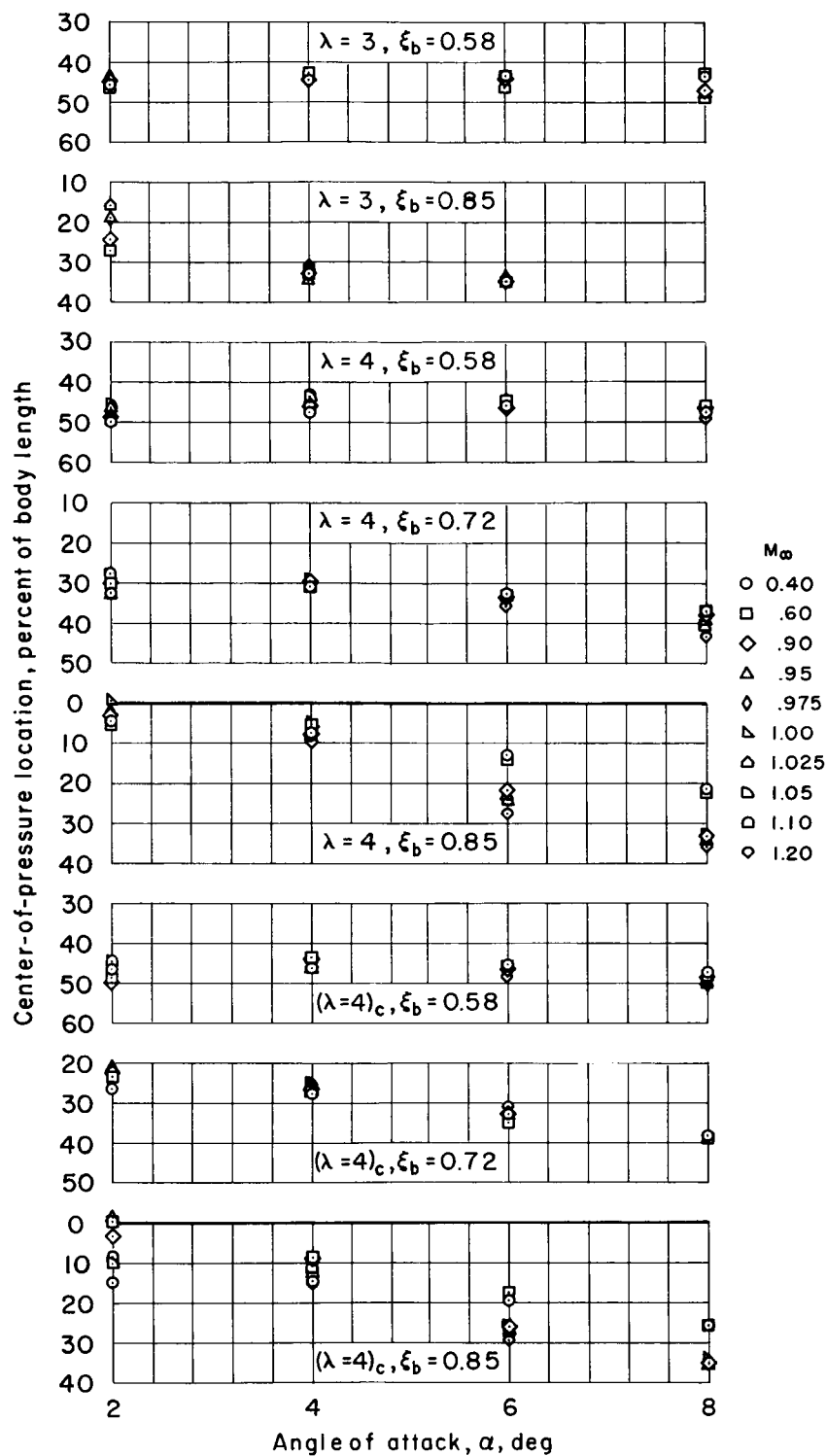
(b) $M_\infty = 1.20$

Figure 20.- Concluded.

Figure 21.- Variation of center-of-pressure location with angle of attack at several Mach numbers.